IET Image Processing

*Research Article*

IET Journals
The Institution of Engineering and Technology

# Scheme for unsupervised colour–texture image segmentation using neutrosophic set and non-subsampled contourlet transform

ISSN 1751-9659
Received on 7th August 2015
Revised on 29th December 2015
Accepted on 23rd January 2016
doi: 10.1049/iet-ipr.2015.0738
www.ietdl.org

*Abed Heshmati*[1] ✉, *Maryam Gholami*[2], *Abdolreza Rashno*[3]

[1]*Department of Computer Engineering and Information Technology, Payame Noor University, Tehran, Islamic Republic of Iran*
[2]*Department of Computer Science, Qorveh Branch, Islamic Azad University, Qorveh, Iran*
[3]*Department of Electrical and Computer Engineering, Isfahan University of Technology, Isfahan, Iran*
✉ *E-mail: abedeheshmatee@gmail.com*

**Abstract:** The process of partitioning an image into some different meaningful regions with the homogeneous characteristics is called the image segmentation which is a crucial task in image analysis. This study presents an efficient scheme for unsupervised colour–texture image segmentation using neutrosophic set (NS) and non-subsampled contourlet transform (NSCT). First, the image colour and texture information are extracted via CIE Luv colour space model and NSCT, respectively. Then, the extracted colour and texture information are transformed into the NS domain efficiently by the authors' proposed approach. In the NS-based image segmentation, the indeterminacy assessment of the images in the NS domain is notified by the entropy concept. The lower quantity of indeterminacy in the NS domain, the higher confidence and easier segmentation could be achieved. Therefore, to achieve a better segmentation result, an appropriate indeterminacy reduction operation is proposed. Finally, the *K*-means clustering algorithm is applied to perform the image segmentation in which the cluster number *K* is determined by the cluster validity analysis. To show the effectiveness of their proposed method, its performance is compared with that of the state-of-the-art methods. The experimental results reveal that their segmentation scheme outperforms the other methods for the Berkeley dataset.

## 1 Introduction

Image segmentation is the process of partitioning a digital image into some different meaningful regions with homogeneous characteristics. It is one of the most crucial tasks in image analysis which is widely used in image processing, computer vision, pattern recognition, medical imaging, digital libraries and image and video retrieval. Specifically, colour–texture segmentation is the task of assigning a label to each pixel according to both colour and texture properties of that pixel. The colour and texture are two fundamental properties used in image segmentation because almost all of the images, especially the natural scene images, contain a combination of these two properties [1].

Generally, the image segmentation algorithms employ two basic properties of intensity values of the image pixels named as discontinuity and similarity. Discontinuity-based image segmentation methods attempt to partition an image by detecting the sharp changes in the image intensity or colour. Algorithms such as Robert, Sobel and Canny edge detectors belong to this category. On the other hand, in similarity-based image segmentation methods, trying to preserve the spatial structure and edge information, the goal is to partition an image into some different regions by grouping the pixels into multiple consistent regions that satisfy some predefined criteria. The region growing and merging methods are two examples of this category.

During the past few decades, a wide variety of image segmentation techniques have been proposed [1–28]. Among them, a particular class is based on multi-resolution analysis. Pyramid-structured wavelet transforms [2] have become an important alternative approach to the multi-resolution analysis. The wavelet transform is a mathematical tool which can be used to describe the images in different resolutions. It is an efficient tool for data approximation, compression and noise removal. The wavelet-based methods can represent functions, sharp peaks and spatial and frequency localisations [3]. Many methods have been proposed in this field [4–10]. Wan *et al.* [4] proposed a new statistical image segmentation method for noisy images based on wavelet transform and Cauchy density. Though it is an efficient method especially for noisy images corrupted by artificial or natural noises, it leads to the over-segmentation. Liapis *et al.* [5] presented a wavelet-based method for image segmentation using both colour and texture features. This method gives satisfactory segmentation results for natural images but the number of colour–texture classes must be selected by the user. Kim and Kim [6] developed a wavelet-based watershed image segmentation method which reduces the over-segmentation phenomenon and is suited for noisy images. Its drawback is that it merges the low-contrast regions incorrectly. Rosito [7] combined the wavelet with watershed segmentation method. This method detects the regions edges properly but it produces the over-segmented objects. Celik and Tjahjadi [8] proposed an effective colour image segmentation algorithm which uses the multi-scale edge information in wavelet domain as well as region growing and merging. Unfortunately, it generates segmentation error if the object edge cannot be detected due to very low contrast between the different regions. Zheng *et al.* [9] improved the multi-resolution Markov random field model using fuzzy constraints in wavelet domain. This method is more suitable for image segmentation but suffers from the problem of under-segmentation. Li [10] proposed a novel fuzzy multiphase image segmentation model based on wavelet regularisation on the membership functions and used principal component analysis (PCA) features as data descriptors. This method has a relatively higher computational complexity and the resulting edges are not smooth.

The wavelet transform has a non-linear estimate performance for the piecewise smooth functions. Though it works well in capturing the point discontinuities, it does not work appropriately in capturing the geometrical smoothness of the curves. To solve this problem, the multi-resolution analysis such as Ridgelet [11], monoscale Ridgelet [12], Curvelet [13] and Contourlet [14] are proposed in order to construct the best estimate performance for

the high-dimension functions. The contourlet transform, presented by Do and Vetterli [14]ta two-dimensional (2D) transform developed for the digital images which is constructed by Laplacian pyramidal and directional filter banks (DFBs). Ning *et al.* presented a novel texture–colour image segmentation method based on colour quantisation and multi-resolution texture characterisation [15]. They used two techniques for region extraction including the wavelet transform for texture and the contourlet transform for boundaries. The main drawback of this method is that it has a high computational complexity.

The contourlet transform is not shift-invariant because of the down-samplers and up-samplers presented in both the Laplacian pyramid and DFBs. To remedy this defect, Da Cunha *et al.* [16] proposed a non-subsampled pyramid structure and a non-subsampled DFB (NSDFB) called non-subsampled contourlet transform (NSCT). Xin *et al.* [17] proposed an unsupervised image segmentation method based on the shift invariance and multidirectional expansion properties of NSCT. This method had a better performance at the edges but a lower missed classed probability. Wang and Zhao [18] devised a new method based on NSCT and bacterial foraging-particle swarm optimisation (PSO) algorithm for image segmentation. A novel approach based on combination of NSCT and marker-controlled watershed was also proposed by Zhang *et al.* [19]. Finally, Li *et al.* [20] proposed an efficient multifocus image fusion scheme in NSCT domain based on the property of optical imaging and the theory of defocused image.

The concept of neutrosophic sets (NSs), discussed by Florentine Smarandache, generalises the concepts of classical set, interval valued fuzzy set, intuitionistic fuzzy set and fuzzy conventional set [21]. The NS is basically a new branch of philosophy which studies the origin and attribute of neutralities in the nature. This mathematical tool is used to solve the problems of vagueness, ambiguity uncertainty, imprecise, indeterminate and inconsistent information which exist in our real world. The quantification of indeterminacy is explicit which is depicted using a membership value. The NS is represented by three membership functions known as truth-membership ($T$), falsity-membership ($F$) and indeterminacy-membership ($I$). The functions $T$, $F$ and $I$ are real standard or non-standard subsets of $]^{-}0,1^{+}[$.

During the past few years, the NS has become an interesting field of study which is used in a variety of different fields such as the growth and decline analysis of the new economies, the financial dataset detection, the relational database systems and the semantic web services [21]. The NS prepares a suitable tool for illustrating the images with uncertain information. Cheng and Guo [22] defined some concepts and operations for image thresholding based on NS which selected the thresholds automatically and effectively. Guo *et al.* [23] employed the NS to process the noisy images and proposed a new neutrosophic approach for image denoising. This method processed not only the noisy images with different levels of noise but also the images with various noise types having no information about the type of the noise. Guo and Cheng [24] also used the NS for image segmentation. Though their method could segment the grey-level images corrupted by different noise levels, its ability to segment the colour–texture images was limited and its parameters were required to be defined manually. Using the watershed method, Zhang *et al.* [25] presented another NS-based segmentation approach. Using their definitions, an image was mapped into the neutrosophic domain. An image segmentation method based on watershed algorithm was then employed in the corresponding domain. In comparison with the traditional edge-based, pixel-based and region-based methods, this algorithm was more robust against the noise. Karabatak *et al.* [26] extended the NS-based image segmentation to colour–texture images and applied $\alpha$-median operator to overcome the blurring effect of the mean operator. The drawbacks of this method are resulting edges are not smooth and producing over-segmentation. Sengur and Guo [27] applied the NS theory into the wavelet transformation theory and proposed a fully automatic approach. Comparing with the new existing methods, their method was able to segment the colour–texture images into more intact details but it did not preserve the smoothness of image edges. Guo and Sengur [28] proposed another new image segmentation algorithm based on neutrosophic similarity clustering which worked only for the grey-level images.

In this paper, we propose a new scheme for unsupervised colour–texture image segmentation using NS and NSCT. First, the colour and texture information of the image are extracted and transformed into the NS domain. The entropy in NS domain is defined and used to assess the indeterminacy of the image in that domain. Then, an entropy-based indeterminacy reduction operation is employed in the NS domain. After that, we apply the $K$-means clustering to finalise the image segmentation. The segmentation results are compared with that of the four other methods including: the unsupervised multi-scale segmentation [29], mean-shift filtering in higher-dimensional space [30], NS and wavelet transformation [27] and modified neutrosophic approach to colour image segmentation [26]. The experimental results reveal that the proposed method outperforms the other methods using different segmentation performance metrics.

The main contributions of this paper are as follows:

(i) Extending the original NS image segmentation proposed in [24] which has some limitations such as: (a) it can only segment the grey-level images. (b) Its ability to segment the colour–texture images is limited and its parameters need to be tuned manually.

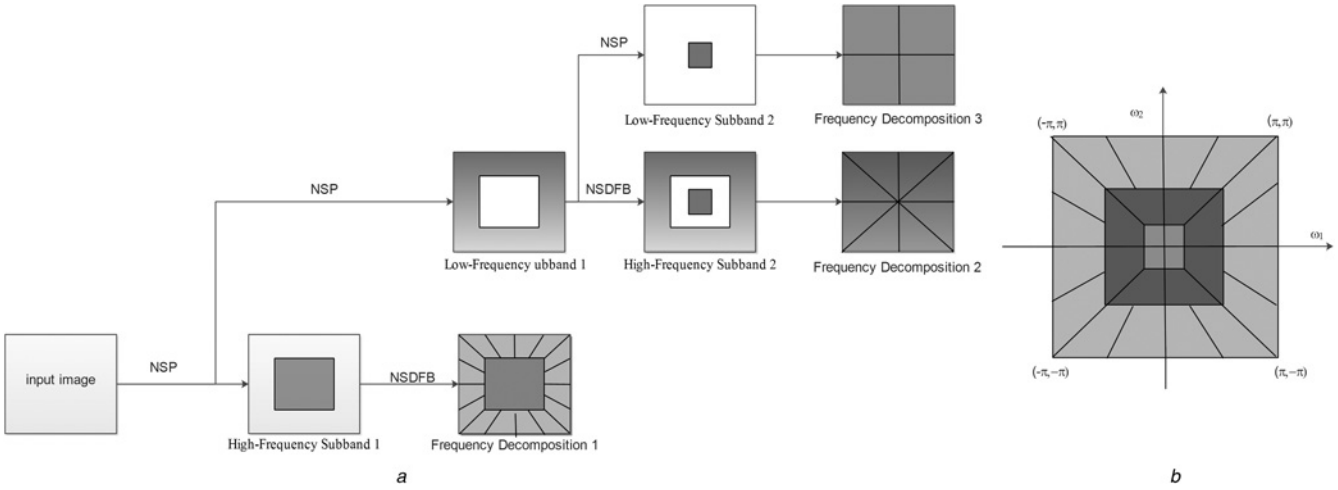


**Fig. 1** *Nonsubsampled contourlet transform*

*a* Two-step decomposition structure of NSCT
*b* Frequency-domain partitioning obtained by the framework proposed in [16]

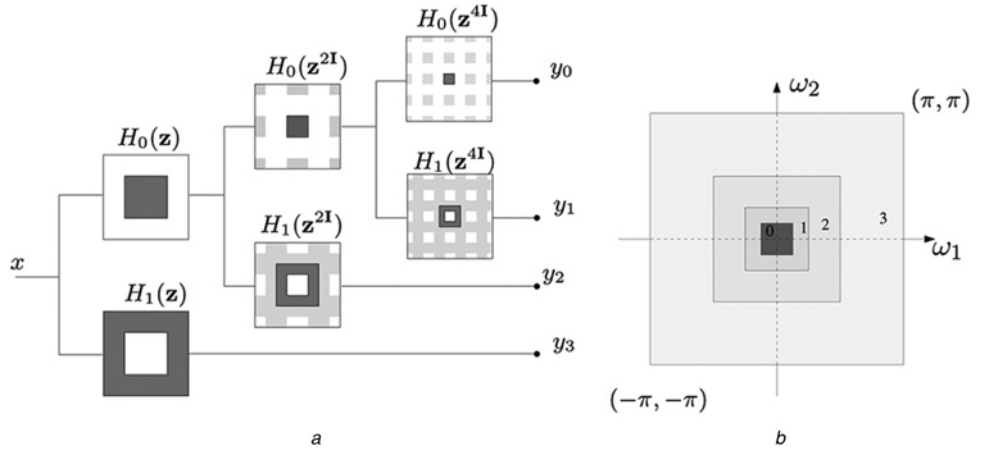


**Fig. 2** *Nonsubsampled pyramid filter bank*

*a* Three-stage non-subsampled pyramid decomposition
*b* Corresponding frequency plane

(ii) Improving the image transformation procedure from pixel domain into NS domain using the histogram and entropy concepts. (iii) Proposing a new indeterminacy reduction operation for enhancing the differences between the intensities and producing more homogenous regions according to the characteristic of the image.

The rest of this paper is organised as follows. In Section 2, the NSCT and NS as well as some preliminaries are presented. Section 3 discusses the methodology of the proposed method, and finally Section 4 gives the experimental results and discussion.

## 2 Preliminaries

In this section, some preliminaries on NSCT and NS are presented.

### 2.1 Non-subsampled contourlet transform

The NSCT scheme is shown in Fig. 1. As seen in this figure, it consists of two shift-invariant parts: the non-subsampled pyramid filter bank (NSPFB) decomposition and NSDFB. The NSPFB enables the non-subsampled multi-scale decomposition and guarantees the multi-scale performance using a two-channel non-subsampled filter bank (NSFB), a low-frequency sub-band and a high-frequency sub-band, which can be manufactured at each NSPFB decomposition level [16, 20]. To achieve the multi-scale decomposition, the filters at the next stage are obtained by up-sampling the filters at the previous stage using the following

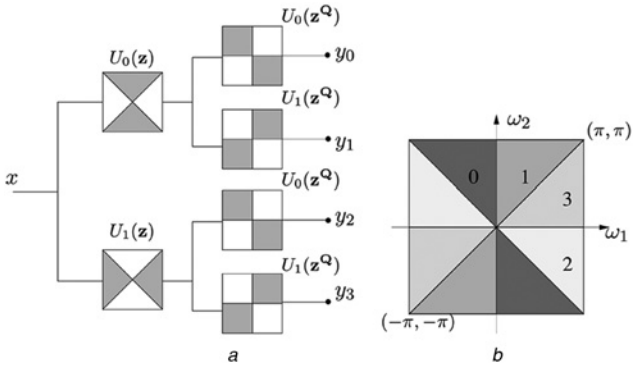


**Fig. 3** *Nonsubsampled directional filter bank*

*a* Four-channels NSDFB built with two-channel fan filter bank
*b* Corresponding frequency plane

sampling matrix

$$\boldsymbol{D} = 2I = \begin{bmatrix} 2 & 0 \\ 0 & 2 \end{bmatrix}.$$

which gives the multi-scale property without requiring any additional filter design. Fig. 2 gives the NSPFB decomposition with $J = 3$ levels. At the $j$th decomposition, the ideal frequency support of the low-pass filter is $[-(\pi/2^j), (\pi/2^j)]^2$. Accordingly, the ideal support of the equivalent high-pass filter is the complement of the low-pass filter, which is $[-(\pi/2^{j-1}), (\pi/2^{j-1})]^2 \backslash [-(\pi/2^j), (\pi/2^j)]^2$. The corresponding filters of the $J$-level cascading NSPFB are given by

$$H_n^{\text{eq}} = \begin{cases} H_1\left(z^{2^{n-1}I}\right) \prod_{j=0}^{n-2} H_0\left(z^{2^j I}\right), & 1 \le n \le j \\ \prod_{j=0}^{n-2} H_0\left(z^{2^j I}\right), & n = j+1 \end{cases} \quad (1)$$

where $H_0(z)$ and $H_1(z)$ denote the corresponding low-pass and high-pass filters, respectively, at the first stage.

The NSDFB enables the non-subsampled directional decomposition and gives the directionality. The NSDFB consists of a two-channel NSFB which are manufactured by wiping the down-samplers and up-samplers and compounding the directional fan filter banks in the non-subsampled directional filter [16]. Fig. 3 illustrates a four-channel NSDFB constructed by two-channel fan filter banks. At the second level, the up-sampled fan filters $U_j(z^{\boldsymbol{Q}})$ ($j = 0, 1$) have checker-board frequency support and the sampling matrix $\boldsymbol{Q}$ is the quincunx matrix, i.e.

$$\boldsymbol{Q} = \begin{bmatrix} 1 & -1 \\ 1 & 1 \end{bmatrix}.$$

When the filters $U_j(z^{\boldsymbol{Q}})$ are combined with the fan filters $U_j(Z)$ ($j = 0, 1$) at the first level, the four-channel directional decomposition is obtained. The equivalent filter in each channel $U_k(Z)$ ($k = 0, 1, 2, 3$) is obtained as

$$U_k(Z) = U_i(Z) U_j(z^{\boldsymbol{Q}}) \quad (2)$$

Higher-level directional decompositions can be produced using the similar strategy but the sampling matrices would become more complex. Hence, all of the filter banks in the NSDFB tree structure are obtained from a single NSFB with fan filters.


*IET Image Process.*, 2016, Vol. 10, Iss. 6, pp. 464–473

Moreover, each filter in the NSDFB tree has the same computational complexity as NSFB.

After a $J$-level NSCT decomposition, a low-pass sub-band image and $\sum_{j=1}^{J} 2^{l_j}$ (in which $l_j$ is the direction of decomposition level at the $j$th scale) band-pass directional sub-band images are obtained whose sizes are the same as the original image.

### 2.2. Neutrosophic set

In [21], the NS and its properties are discussed. Let $X$ be a universal set in the NS domain. Each element in $X$ can be expressed in terms of a set $A$ with three subsets named $T$, $I$ and $F$ as neutrosophic components to represent $\{A\}$, $\{Neut\text{-}A\}$ and $\{Anti\text{-}A\}$. Let $T$, $I$ *and* $F$ be the real standard or non-standard subsets of [0, 1] with $Sup\_T = t\_sup$, $inf\_T = t\_inf$, $Sup\_I = i\_sup$, $inf\_I = i\_inf$, $Sup\_F = f\_sup$, $inf\_F = f\_inf$, $n\text{-}sup = t\_sup + i\_sup + f\_sup$, $n\text{-}inf = t\_inf + i\_inf + f\_inf$. Hence, a sentence can be expressed by $A = (t, i, f)$ which means that the sentence is true with probability of $\%t$, uncertain with probability of $\%i$ and false with probability of $\%f$.

### 2.3. Neutrosophic image

To apply the concept of NS to image processing problems, an image should be transferred into the neutrosophic domain. Image $P$ of size $M \times N$ with $L$ grey levels can be defined as three arrays of neutrosophic images described by three membership sets $T$ (true subset), $I$ (indeterminate subset) and $F$ (false subset). Therefore, the pixel $P(i, j)$ in the image domain transferred into the neutrosophic domain can be represented by $P_{\mathrm{NS}}(i, j) = \{T(i, j), I(i, j), F(i, j)\}$ or $P_{\mathrm{NS}}(t, i, f)$. It means that the pixel is $\%t$ true, $\%i$ indeterminate and $\%f$ false. Here, $t$ varies in $T$ (white pixel set), $i$ varies in $I$ (noise pixel set) and $f$ varies in $F$ (black pixel set) which are defined as follows [24]

$$T(i, j) = \frac{\overline{g(i, j)} - \overline{g_{\min}}}{\overline{g_{\max}} - \overline{g_{\min}}} \tag{3}$$

$$F(i, j) = 1 - T(i, j) \tag{4}$$

$$I(i, j) = \frac{\delta(i, j) - \delta_{\min}}{\delta_{\max} - \delta_{\min}} \tag{5}$$

$$\overline{g(i, j)} = \frac{1}{w^2} \sum_{m=-w/2}^{m=w/2} \sum_{n=-w/2}^{n=w/2} g(i+m, j+n) \tag{6}$$

$$\delta(i, j) = \left| g(i, j) - \overline{g(i, j)} \right| \tag{7}$$

In these equations, $g$ represents the grey-scale image, $g(i, j)$ is the intensity value of the pixel $P(i, j)$, $\overline{g(i, j)}$ is the local mean value of the $g(i, j)$, $w$ is the size of the sliding window and $\overline{g_{\max}}$ and $\overline{g_{\min}}$ are the maximum and minimum of the local mean values in the image, respectively. $\delta(i, j)$ is the absolute value of the difference between the intensity $g(i, j)$ and the local mean value $\overline{g(i, j)}$ of the pixel $P(i, j)$ assuming that it is processed by a kernel with the expanse of $w$. $\delta_{\max}$ and $\delta_{\min}$ are also the maximum and minimum values of $\delta(i, j)$in the whole image, respectively.

The entropy is used to evaluate the distribution of pixels in the grey-level images. The uniform intensity distributions correspond to the high-entropy values, whereas the non-uniform intensity distributions correspond to the low-entropy values. For the neutrosophic images, the entropy is defined as the summation of the entropies of three subsets $T$, $F$ and $I$

$$\mathrm{En}_{\mathrm{NS}} = \mathrm{En}T + \mathrm{En}F + \mathrm{En}I \tag{8}$$

$$\mathrm{En}T = -\sum_{i=1}^{h} \sum_{j=1}^{w} T(i, j) \log_2 T(i, j) \tag{9}$$

$$\mathrm{En}F = -\sum_{i=1}^{h} \sum_{j=1}^{w} F(i, j) \log_2 F(i, j) \tag{10}$$

$$\mathrm{En}I = -\sum_{i=1}^{h} \sum_{j=1}^{w} I(i, j) \log_2 I(i, j) \tag{11}$$

In these equations, $\mathrm{En}_{\mathrm{NS}}$ is the entropy of the image in the neutrosophic domain. En$T$, En$F$ and En$I$ are also the entropies of subsets $T$, $F$ and $I$, respectively. $h$ and $w$ represent the height and width of the image, respectively.

## 3 Proposed method

### 3.1 Transforming the image into NS

In this paper, we improve the transformation part proposed in [24] as follows

$$T(i, j) = \frac{\overline{g(i, j)} - \overline{g_{\min}}}{\overline{g_{\max}} - \overline{g_{\min}}} \tag{12}$$

$$I(i, j) = -\sum_{m=-(w/2)}^{m=w/2} \sum_{n=-(w/2)}^{n=w/2} \left( \mathrm{His}\, g(i+m, j+n) \times \log_2 \mathrm{His}\, g(i+m, j+n) \right) \tag{13}$$

$$F(i, j) = 1 - T(i, j) - I(i, j) \tag{14}$$

$$\overline{g(i, j)} = \frac{1}{w^2} \sum_{m=-(w/2)}^{m=w/2} \sum_{n=-(w/2)}^{n=w/2} g(i+m, j+n) \tag{15}$$

where $g$ is the grey-scale image, $g(i, j)$ is the intensity value of the pixel $P(i, j)$, $\overline{g(i, j)}$ is the local mean value of the $g(i, j)$, $w$ is the size of the sliding window, $\overline{g_{\max}}$ and $\overline{g_{\min}}$are the maximum and minimum values of the local mean values in the image, respectively, and $His(m, n)$ is the histogram of the image for pixel $(m, n)$.

To measure the indeterminacy of pixels in $P_{\mathrm{NS}}(i, j)$, the value of $I(i, j)$ is employed. For this purpose, the histogram and entropy concepts are used. Specifically, we obtain the image histogram and then calculate the entropy from that.

At the first step, the images are transformed from red-green-blue (RGB) to grey-level space for texture feature extraction. Then, the grey-scale images are decomposed using the NSCT. As mentioned in Section 2.1, the NSCT decomposition is based on NSP and NSDFB. The effect of the various NSP and NSDFB on the performance of the segmentation methods is also analysed in this paper. For this analysis, we consider the different kinds of NSP: namely, '*maxflat*' (derived from 1D filters using a maximally flat mapping function with four vanishing moments), '9–7' (derived from 9 to 7 1D prototypes), '*pyr*' (derived from 1D filters using a maximally flat mapping function with two vanishing moments), '*pyrexc*' (same as *pyr* but exchanging the two high-pass filters) and different kinds of NSDFB: namely, '*dmaxflat*' (diamond *maxflat* filters obtained from a three-stage ladder), '*pkva*' (ladder filters by Phong *et al.*), '*cd*' (derived from 9 to 7 *biorthogonal* filters using McClellan transformed by Cohen and Daubechies) and '*vk*' (McClellan transformed of the filter from the VK book). On the basis of our experiments, the best results are achieved in '9–7' and '*pkva*' for NSP and NSDFB, respectively. Here, a three-level NSCT decomposition is done where one sub-band at

the first level, two sub-bands at the second level, eight sub-bands at the third level and one low-pass sub-band with low-frequency components are considered. Among the obtained sub-bands, the first two ones at the third level are called *SBL*31 and *SBL*32. Most of the texture information is included at these sub-bands. Since their coefficients are entirely sparse,applying some types of window operations to these sub-bands are needed in order to obtain a more uniform texture characterisation. The means of *SBL*31 and *SBL*32 sub-bands in a local window are calculated as follows

$$MSBL31 = \frac{1}{w^2} \sum_{m=-(w/2)}^{m=w/2} \sum_{n=-(w/2)}^{n=w/2} SBL31(i+m, j+n) \quad (16)$$

$$MSBL32 = \frac{1}{w^2} \sum_{m=-\frac{w}{2}}^{m=\frac{w}{2}} \sum_{n=-\frac{w}{2}}^{n=\frac{w}{2}} SBL32(i+m, j+n) \quad (17)$$

where $w$ is the size of the sliding window (which is experimentally set to 5). *MSBL*31 and *MSBL*32 are then transformed into the NS domain using (12)–(15).

At the second step, the RGB colour input image is converted into the CIE Luv colour space for extracting the colour information. $L$, $u$ and $v$ channels are then transformed into the NS domain using (12)–(15), independently.

### 3.2 Indeterminacy reduction

Among the three subsets obtained at the previous section, $T$ subset is needed to perform the extra processing. To enhance the differences between the intensities and produce more homogenous regions, an indeterminacy reduction operation is required to be performed on the $T$ subset. This operation reduces the image indeterminacy using the entropy concept. To this end, we propose to use the following equations

$$\bar{P}_{\mathrm{NS}}(\eta) = \{ \bar{T}(\eta), \bar{F}(\eta), \bar{I}(\eta) \} \quad (18)$$

$$\bar{T}(\eta) = \begin{cases} T(i,j) & I(i,j) < \eta \\ T'_{\eta}(i,j) & I(i,j) \geq \eta \end{cases} \quad (19)$$

$$T'_{\eta}(i,j) = \begin{cases} 2T^2(i,j) & T(i,j) \leq \eta \\ \frac{1}{1-\eta}\left[1 - 2\left(1 - T(i,j)\right)^2\right] & T(i,j) > \eta \end{cases} \quad (20)$$

$$\bar{F}(\eta) = \begin{cases} F(i,j) & I(i,j) < \eta \\ F'_{\eta}(i,j) & I(i,j) \geq \eta \end{cases} \quad (21)$$

$$F'_{\eta}(i,j) = \begin{cases} 2F^2(i,j) & F(i,j) \leq \eta \\ \frac{1}{1-\eta}\left[1 - 2\left(1 - F(i,j)\right)^2\right] & F(i,j) > \eta \end{cases} \quad (22)$$

$$\bar{I}(\eta) = -\sum_{m=-(w/2)}^{m=w/2} \sum_{n=-(w/2)}^{n=w/2} \left(\mathrm{His}\bar{T}(i+m, j+n) \times \log_2 \mathrm{His}\bar{T}(i+m, j+n)\right) \quad (23)$$

where $\bar{P}_{\mathrm{NS}}(\eta)$ is the neutrosophic image after indeterminacy reduction. $\eta$ is also a parameter determined by entropy of the image which is defined as follows

$$\eta = c\left(1 + \frac{SEnI}{\log(1/hw)}\right) \quad (24)$$

In (24), $h$ and $w$ are the height and width of the image, respectively, and $c = 0.99$ which is determined experimentally. Finally, *SEnI* is calculated as follows

$$SEnI = \sum_{sb=1}^{\text{number of indeterminacy sub-bunds}} EnI_{sb} \quad (25)$$

The indeterminacy reduction operation is applied repeatedly until the overall entropy reduction rate of this set reaches a threshold. This operation increases the true subset contrast which causes this set to be more district and therefore more suitable for segmentation.

### 3.3 Apply K-means clustering on NS

At the final stage of our method, the true subsets of $L$, $u$, $v$, *SBL*31 and *SBL*32 channels are combined into a matrix column to be used as the input of clustering. In this paper, we use the $K$-means clustering algorithm which is one of the most popular and efficient methods in image segmentation domain. This algorithm minimises the following objective function

$$J = \sum_{l=1}^{K} \sum_{i=1}^{H} \sum_{j=1}^{W} T_{\mathrm{all}}(i,j) - Z_l^2 \quad (26)$$

$$Z_l = \frac{1}{n_l} \sum_{T_{\mathrm{all}}(i,j) \in C_l} T_{\mathrm{all}}(i,j) \quad (27)$$

where $J$ is the compactness measure, $Z_l$ is the centre of the cluster $C_l$, $n_l$ is the number of data in the cluster $C_l$ and $K$ represents the total number of clusters. We use the idea proposed in [31] to obtain the number of clusters automatically as follows

$$S_{XB}(K) = \frac{J}{n \times min_{i,j} Z_i - Z_j^2} \quad (28)$$

where $n$ is the number of data to be clustered. To achieve the best clustering performance for the dataset, one can obtain an optimal $K^*$ by solving the following equation

$$K^* = \min_{2 \leq k \leq n-1} S_{XB}(K) \quad (29)$$

The proposed algorithm is illustrated in Fig. 4.

## 4 Experimental results and discussion

Our proposed method is evaluated using the well-known Berkeley segmentation dataset (BSD) [32]. This dataset contains the hand-labelled segmentations of the images by 30 human subjects. It is widely used for benchmarking the image segmentation and boundary detection algorithms. The BSD consists of the various images from the Corel dataset and includes the ground-truth of 300 images of size $481 \times 321$ pixels. The images contain landscapes, animals, portraits and various objects.

Evaluating the performance of the image segmentation methods is a challenging task because defining a universally accepted objective criterion is almost impossible. However, the following metrics can be used to evaluate the performance of the image segmentation methods:

- F-measure (or F1-score) [33] which is a single goodness measure based on the combination of precision ($P$) and recall ($R$). It is defined as

$$F = \frac{P.R}{\varepsilon.P + (1-\varepsilon).R} \quad (30)$$

where $\epsilon$ denotes the trade-off between $P$ and $R$ which is set to 0.5. To calculate $P$ and $R$, the edges of the obtained segments are thinned.


*IET Image Process.*, 2016, Vol. 10, Iss. 6, pp. 464–473

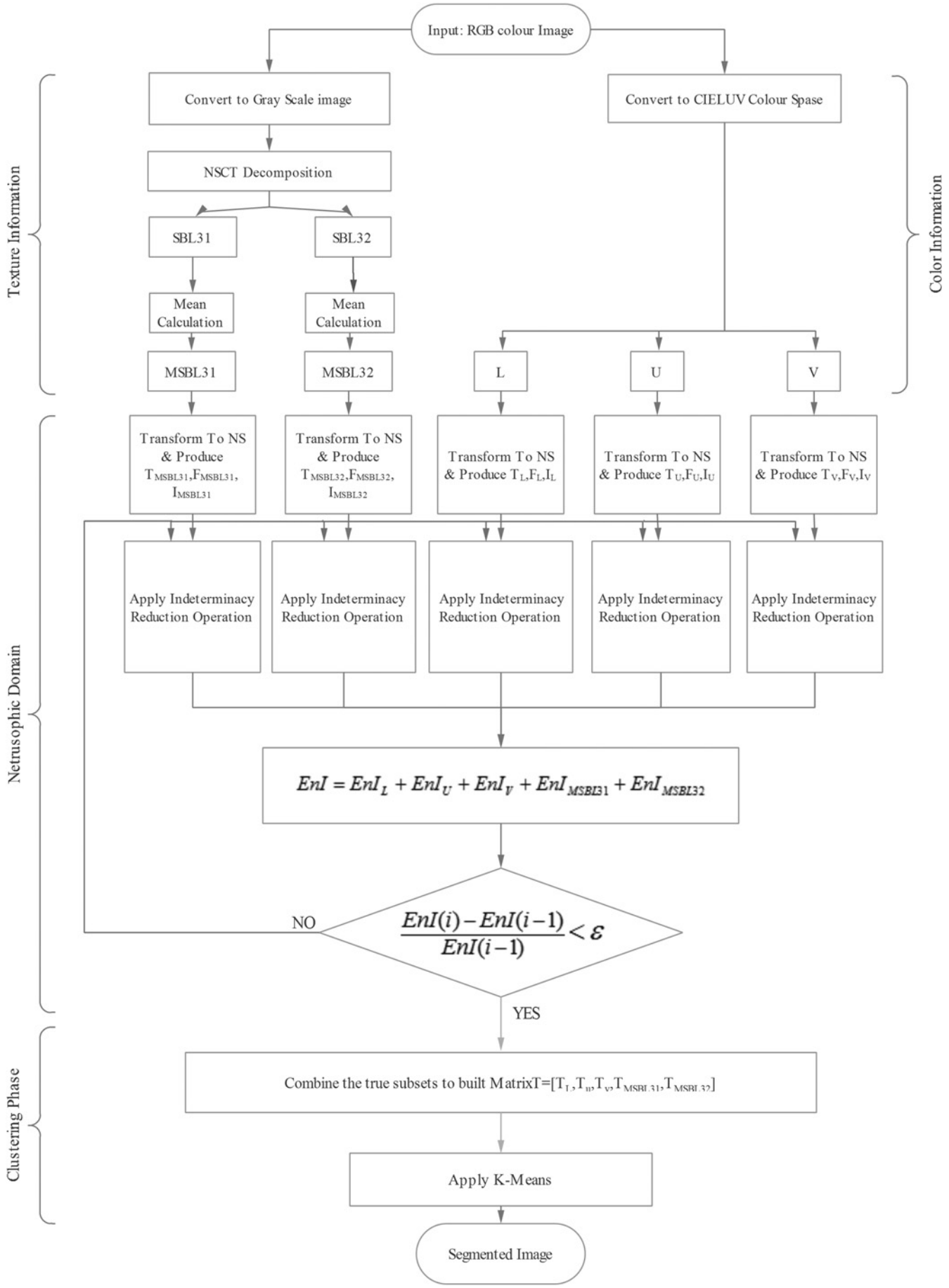


**Fig. 4** *Flowchart of the proposed method*

These edges are then matched to the ground-truth. $P$ and $R$ are then calculated based on these matches as follows

$$P = \frac{t_p}{t_p + f_p} \tag{31}$$

$$R = \frac{t_p}{t_p + f_n} \tag{32}$$

where $t_p$ (true positive) and $f_p$ (false positive) are the numbers of correctly and falsely segmented pixels, respectively. $f_n$ (False negative) is the number of the missed pixels in the segmentation result.

- Error rate (ER) average normal precision [34, 35] which is defined as the ratio of misclassified image pixels to the total number of image pixels as

$$\mathrm{ER} = \frac{f_p + f_n}{N_t} \times 100\%. \tag{33}$$

In (33), $N_t$ is the total number of image pixels, $t_p$ and $f_p$ are the numbers of correctly and falsely segmented pixels, respectively and $f_n$ is the number of the missed pixels in the segmentation result.

- Pratt's figure of merit (FOM) [36] which is one of the most frequently used methods for evaluating the performance of the edge detectors quantitatively. It is computed as

$$\mathrm{FOM} = \frac{1}{\max(N_I,\ N_D)} \sum_{i=1}^{N_D} \frac{1}{1 + \alpha d_i^2} \tag{34}$$

where $N_I$ and $N_D$ represent the numbers of detected edge points and the ground-truth edges, respectively. The parameter max ($N_I$, $N_D$) penalises the number of missing edges. $\alpha$ is also a scaling factor which is set to 1/9 for the obtained results. It provides a relative weighting between the smeared and the thin but offset edges. $d_i$ is the distance between the point declared as an edge point and the nearest ideal edge point.

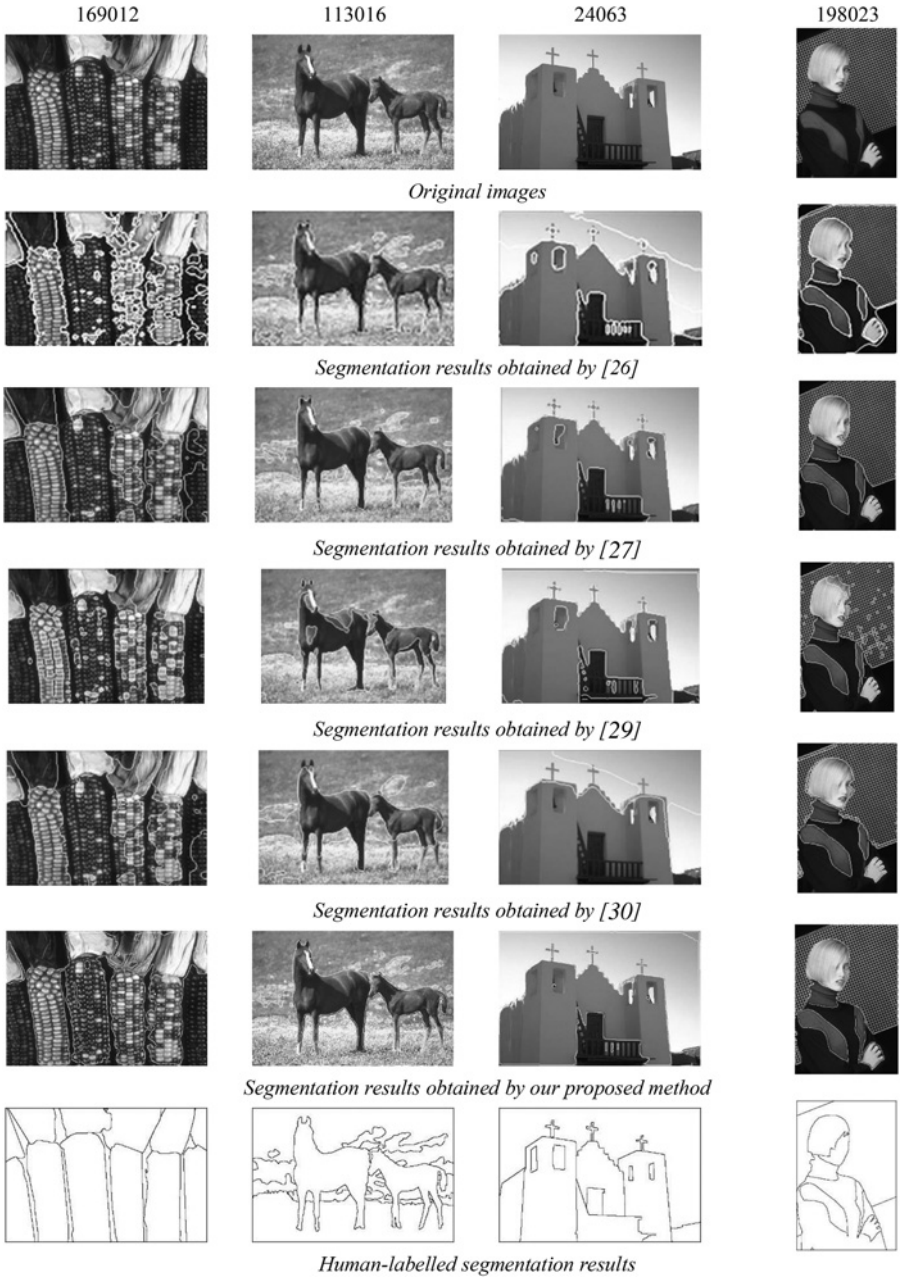


**Fig. 5** *Segmentation results of the human-labelled and the other different segmentation methods*

Original images; segmentation results obtained by [27]; segmentation results obtained by [28]; segmentation results obtained by [30]; segmentation results obtained by [31]; segmentation results obtained by our proposed method; and human labelled segmentation results


*IET Image Process.*, 2016, Vol. 10, Iss. 6, pp. 464–473

To evaluate the performance of our proposed method, we compare it with some other image segmentation methods including the unsupervised multi-scale segmentation [29], the image segmentation by mean-shift filtering in higher-dimensional space [30] and image segmentation using NS and wavelet transformation [27].

The visual comparison of the proposed image segmentation method with those proposed in [26, 27, 29, 30] and the human-labelled segmentations is provided in Figs. 5 and 6. In these figures, the first row presents the original images as well as their ID numbers in dataset. The second, third, fourth and fifth rows present the segmentation results of the methods proposed in [26, 27, 29, 30], respectively. The results of our proposed method are presented at the sixth row, and finally the seventh row presents the human-labelled segmentation results.

To illustrate the performance of the proposed algorithm, two images including '169012' (called 'corn') and '134008' (called 'cheetah') are considered.

It can be seen that the segmentation method proposed in [26, 29] has the worst result for the corn image in which the over-segmentation is obvious. The methods proposed in [27, 30] almost have the similar results. Though [27, 30] give the less accurate segmentation results in comparison with the human-labelled segmentation, they outperform the methods of [26, 29]. The results also reveal that our proposed method considerably improves the segmentation accuracy comparedwith the other methods. Beside the numerical segmentation results, an obvious prove for this claim is depicted in the corn image segmentation. According to Fig. 5, it is obvious that our proposed method is by far the best segmentation algorithm which leads to an exact segmentation of the corn body and the case while none of the three mentioned methods could segment it accurately.

Another image used for the evaluation of segmentation algorithms is 'cheetah'. This image can be divided into the background region and cheetah region as shown in the human-labelled segmentation image in Fig. 6.

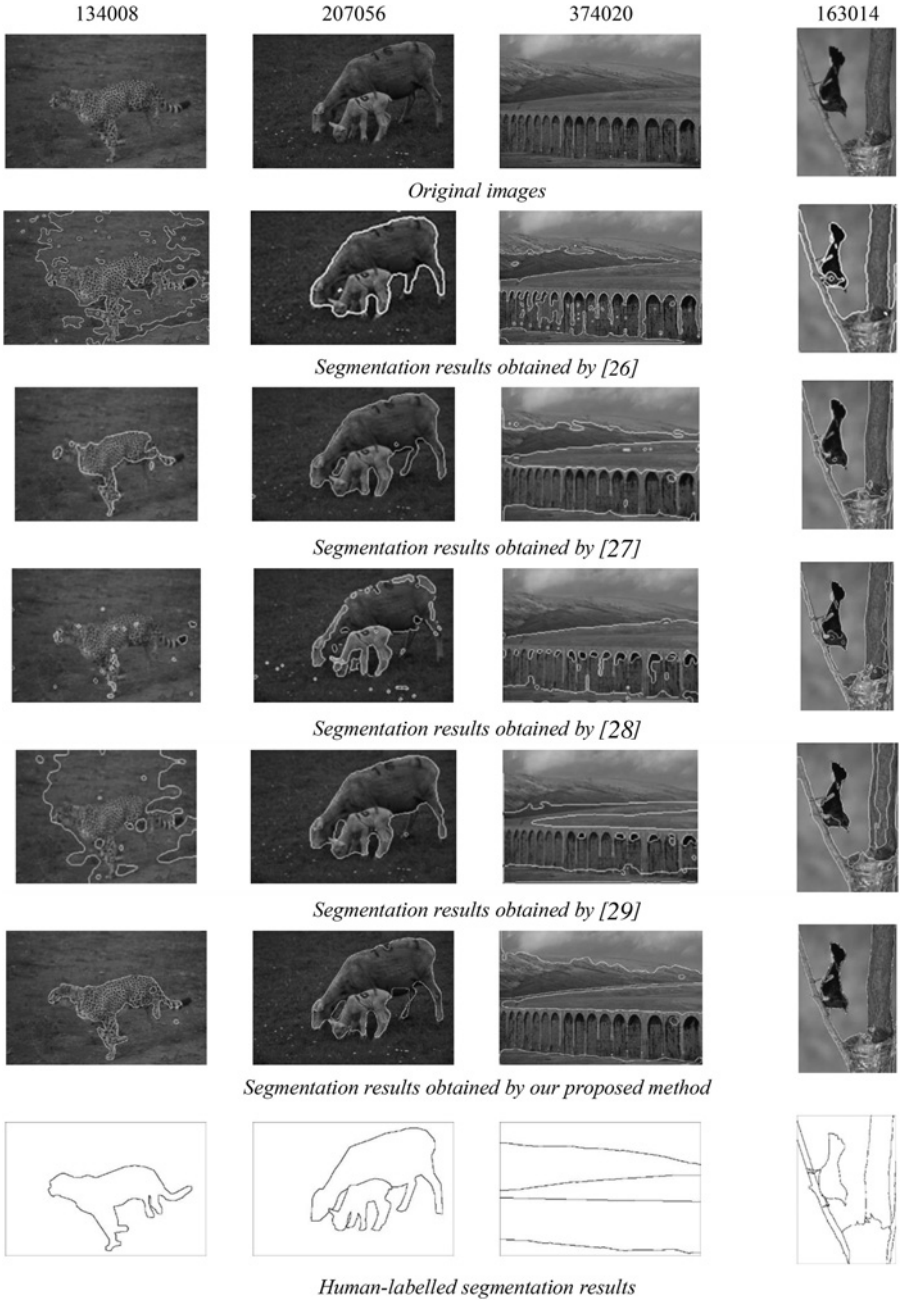


**Fig. 6** *Segmentation results of human-labelled and the other different segmentation methods*

Original images; segmentation results obtained by [27]; segmentation results obtained by [28]; segmentation results obtained by [30]; segmentation results obtained by [31]; segmentation results obtained by our proposed method; and human labelled segmentation results

**Table 1** Quantitative comparison between the proposed and the other segmentation methods

| BSD test image number | | 169012 | 113016 | 24063 | 198023 | 134008 | 207056 | 374020 | 163014 |
|---|---|---|---|---|---|---|---|---|---|
| The quantitative comparison between the proposed and the other segmentation methods | | | | | | | | | |
| **F-measure** | scheme [26] | 0.5246 | 0.8385 | 0.7244 | 0.8261 | 0.5201 | 0.8242 | 0.5388 | 0.8517 |
| | scheme [27] | 0.6128 | 0.8385 | 0.8196 | **0.9126** | 0.6937 | **0.8974** | 0.7478 | **0.8817** |
| | scheme [29] | 0.3354 | 0.5433 | **0.8246** | 0.7612 | 0.2176 | 0.7989 | 0.5178 | 0.7890 |
| | scheme [30] | 0.5818 | 0.7390 | 0.6782 | 0.8987 | 0.4194 | 0.8438 | 0.6390 | 0.8542 |
| | proposed method | **0.6316** | **0.8664** | 0.8112 | 0.8707 | **0.7108** | 0.8514 | **0.8362** | 0.8444 |
| **FOM** | scheme [26] | 0.3684 | 0.4503 | 0.3405 | 0.3139 | 0.2320 | 0.3677 | 0.2816 | 0.4124 |
| | scheme [27] | 0.4134 | 0.4572 | 0.4976 | 0.5974 | 0.3921 | 0.5514 | 0.4453 | 0.6398 |
| | scheme [29] | 0.3339 | 0.3767 | 0.5896 | 0.5619 | 0.1738 | 0.4494 | 0.3720 | 0.5776 |
| | scheme [30] | 0.3774 | 0.3341 | 0.2003 | 0.5714 | 0.1811 | 0.4809 | 0.3334 | 0.4243 |
| | proposed method | **0.5225** | **0.6341** | **0.5956** | **0.7800** | **0.6315** | **0.7779** | **0.5367** | **0.7959** |
| **ER** | scheme [26] | 42.11% | 18.98% | 14.67% | 16.31% | 75.04% | 24.82% | 17.09% | 12.63% |
| | scheme [27] | 38.46% | 19.23% | 16.33% | 12.51% | 18.67% | **22.50%** | 13.76% | 10.21% |
| | scheme [29] | 53.69% | 31.92% | 15.33% | 20.16% | 63.12% | 57.48% | 37.62% | 29.19% |
| | scheme [30] | 34.61% | 25.38% | 20.66% | 17.47% | 72.15% | 40.14% | 23.75% | 15.32% |
| | proposed method | **26.92%** | **16.53%** | **12.12%** | **13.12%** | **9.37%** | 26.27% | **8.46%** | **7.19%** |

The significance of the bold values in Table 1 is that they are the maximum values among other ones for a measure in each column. This shows which method has the maximum value in each image.

As for the corn image, the method proposed in [29] gives the worst segmentation result in which almost the whole image is labelled as background region. Furthermore, in the result obtained by Karabatak *et al.* [26] and Ozden and Polat [30], the cheetah region is not found and some parts of the background region are labelled as the cheetah region. The background region is obtained clearly by Sengur and Guo [27] but some parts of the cheetah region such as its head are wrongly segmented. It is obvious that our proposed method produces the better segmentation results compared with the other methods though the whole cheetah region is not correctly segmented.

The quantitative evaluation using F-measure, ER and FOM metrics is reported in Table 1 for five different image segmentation methods. Though for our proposed method, the F-measure metric is not at the best level for images 24063, 198023, 207056 and 163014, the FOM metric is the largest for all images. Furthermore, the proposed method has the lower ER in comparison with the other methods except for image 207056. These results show that our proposed method significantly outperforms the other methods for the majority of test images.

## 5 Conclusion

In this paper, a novel colour–texture image segmentation algorithm is introduced which uses the NS and NSCT. The NS domain operations are improved and an effective indeterminacy reduction operation is proposed. The colour channels and the NSCT domain features of the input colour–texture image are transformed into the NS domain independently. The colour channels are extracted from the CIE Luv colour space model. A three-level NSCT decomposition is applied to the grey-scale image and a local mean window operation is applied to the NSCT coefficients.

Finally, all true subsets in the NS domain are combined for *K*-means clustering algorithm. The algorithm is applied to the BSD and the outcomes are evaluated using three metrics: namely, F-measure, ER and FOM. The proposed method is compared with the four state-of-the-art image segmentation algorithms. The experimental results show that the proposed method has the superior performance. Since it is not sensitive to noise, the proposed image segmentation scheme could also be adapted and used in the medical image segmentation applications. For example, by a simple extension of our proposed method, the abnormal regions and their boundaries could efficiently be segmented from the background in the medical images. Unfortunately, the segmentation results are so sensitive to the algorithm parameters. In this paper, the parameters are tuned experimentally. However, these parameters could optimally be tuned using an optimisation algorithm such as PSO. In PSO, the cost function could be defined as the segmentation accuracy. The goal is to maximise the cost function where the variables are the algorithm parameters. Finally, as an extension to our algorithm, other clustering methods such as graph-based clustering could be used instead of a simple *K*-means. In the graph-based clustering, the spatial aspect of the pixels is considered. So, the segmentation errors could be decreased consequently.

## 6 References


1 Cheng, H.D., Jiang, X.H., Sun, Y., *et al.*: 'Color image segmentation: advances and prospects', *Pattern Recognit.*, 2001, **34**, (12), pp. 2259–2281
2 Mallat, S.G.: 'A theory for multiresolution signal decomposition: the wavelet representation', *IEEE Trans. Pattern Anal. Mach. Intell.*, 1989, **11**, (7), pp. 674–693
3 Meyer, Y.: 'Wavelets-algorithms and applications'. Wavelets-Algorithms and applications Society for Industrial and Applied Mathematics Translation., 1993, p. 142
4 Wan, T., Canagarajah, N., Achim, A.: 'Segmentation of noisy colour images using Cauchy distribution in the complex wavelet domain', *IET Image Process.*., 2011, **5**, (2), pp. 159–170
5 Liapis, S., Sifakis, E., Tziritas, G.: 'Colour and texture segmentation using wavelet frame analysis, deterministic relaxation, and fast marching algorithms', *J. Vis. Commun. Image Represent.*, 2004, **15**, (1), pp. 1–26
6 Kim, J.B., Kim, H.J.: 'Multiresolution-based watersheds for efficient image segmentation', *Pattern Recognit. Lett.*, 2003, **24**, (1), pp. 473–488
7 Jung, C.R.: 'Combining wavelets and watersheds for robust multiscale image segmentation', *Image Vis. Comput.*, 2007, **25**, (1), pp. 24–33
8 Celik, T., Tjahjadi, T.: 'Unsupervised colour image segmentation using dual-tree complex wavelet transform', *Comput. Vis. Image Underst.*, 2010, **114**, (7), pp. 813–826
9 Zheng, C., Qin, Q., Liu, G., *et al.*: 'Image segmentation based on multiresolution Markov random field with fuzzy constraint in wavelet domain', *IET Image Process.*., 2012, **6**, (3), pp. 213–221
10 Li, Y.: 'Wavelet-based fuzzy multiphase image segmentation method', *Pattern Recognit. Lett.*, 2015, **53**, pp. 1–8
11 Candes, E.J.: 'Ridgelets: theory and applications'. Doctoral dissertation, Stanford University, 1998
12 Candes, E.J.: 'Monoscale ridgelets for the representation of images with edges'. Technical Report, Department of Statistics, Stanford University, Stanford, CA, 1999
13 Starck, J.L., Candes, E.J., Donoho, D.L.: 'The curvelet transform for image denoising', *IEEE Trans. Image Process.*, 2002, **11**, (6), pp. 670–684
14 Do, M.N., Vetterli, M.: 'The contourlet transform: an efficient directional multiresolution image representation', *IEEE Trans. Image Process.*, 2005, **14**, (12), pp. 2091–2106
15 An, N.Y., Pun, C.M.: 'Color image segmentation using adaptive color quantization and multiresolution texture characterization', *Signal Image Video Process.*, 2014, **8**, (5), pp. 943–954
16 Da Cunha, A.L., Zhou, J., Do, M.N.: 'The nonsubsampled contourlet transform: theory, design, and applications', *IEEE Trans. Image Process.*, 2006, **15**, (10), pp. 3089–3101
17 Xin, F., Jiao, L., Wan, H.: 'Unsupervised image segmentation based on nonsubsampled contourlet hidden Markov trees model'. Second Asian-Pacific Conf. on Synthetic Aperture Radar, Xian, China, 2009, pp. 485–488
18 Wang, L., Zhao, Z.: 'Image segmentation based on NSCT and BF-PSO algorithm'. in Sun, C., Fang, F., Zhou, Z.H., Yang, W., Liu, Z.Y. (Eds.): 'Intelligence science and big data engineering' (Springer, Berlin, Heidelberg, 2013), pp. 303–311
19 Zhang, X., Song, J., Yi, Z., *et al.*: 'Image segmentation based on NSCT and watershed'. ICIEA: Fourth IEEE Conf. Industrial Electronics and Applications, Xian, China, May 2009, pp. 3054–3057

20 Li, X., Li, H., Yu, Z., *et al*.: 'Multifocus image fusion scheme based on the multiscale curvature in nonsubsampled contourlet transform domain', *Opt. Eng.*, 2015, **54**, (7), p. 073115
21 Smarandache, F.: 'A unifying field in logics neutrosophic logic. Neutrosophy, neutrosophic set, neutrosophic probability' (American Research Press, New York, 2003)
22 Cheng, H.D., Guo, Y.: 'A new neutrosophic approach to image thresholding', *New Math. Nat. Comput.*, 2008, **4**, (03), pp. 291–308
23 Guo, Y., Cheng, H.D., Zhang, Y.: 'A new neutrosophic approach to image denoising', *New Math. Nat. Comput.*, 2009, **5**, (03), pp. 653–662
24 Guo, Y., Cheng, H.D.: 'New neutrosophic approach to image segmentation', *Pattern Recognit.*., 2009, **42**, (5), pp. 587–595
25 Zhang, M., Zhang, L., Cheng, H.D.: 'A neutrosophic approach to image segmentation based on watershed method', *Signal Process.*., 2010, **90**, (5), pp. 1510–1517
26 Karabatak, E., Guo, Y., Sengur, A.: 'Modified neutrosophic approach to color image segmentation', *J. Electron. Imaging*, 2013, **22**, (1), p. 013005
27 Sengur, A., Guo, Y.: 'Color texture image segmentation based on neutrosophic set and wavelet transformation', *Comput. Vis. Image Underst.*, 2011, **115**, (8), pp. 1134–1144
28 Guo, Y., Şengür, A.: 'A novel image segmentation algorithm based on neutrosophic similarity clustering', *Appl. Soft Comput.*, 2014, **25**, pp. 391–398
29 Jung, C.R.: 'Unsupervised multiscale segmentation of color images', *Pattern Recognit. Lett.*, 2007, **28**, (4), pp. 523–533
30 Ozden, M., Polat, E.: 'A color image segmentation approach for content-based image retrieval', *Pattern Recognit.*, 2007, **40**, (4), pp. 1318–1325
31 Xie, X.L., Beni, G.: 'A validity measure for fuzzy clustering', *IEEE Trans. Pattern Anal. Mach. Intell.*, 1991, **13**, (8), pp. 841–847
32 The Berkeley Segmentation Dataset Benchmark. Available at http://www.eecs.berkeley.edu/Research/Projects/CS/vision/grouping/segbench/, University of California, Berkeley, CA, USA, 2003
33 Martin, D.R., Fowlkes, C.C., Malik, J.: 'Learning to detect natural image boundaries using local brightness, color, and texture cues', *IEEE Trans. Pattern Anal. Mach. Intell.*, 2004, **26**, (5), pp. 530–549
34 Unnikrishnan, R., Pantofaru, C., Hebert, M.: 'Toward objective evaluation of image segmentation algorithms', *IEEE Trans. Pattern Anal. Mach. Intell.*, 2007, **29**, (6), pp. 929–944
35 Estrada, F.J., Jepson, A.D.: 'Benchmarking image segmentation algorithms', *Int. J. Comput. Vis.*, 2009, **85**, (2), pp. 167–181
36 Abdou, I.E., Pratt, W.K.: 'Quantitative design and evaluation of enhancement/thresholding edge detectors', *Proc. IEEE*, 1979, **67**, (5), pp. 753–763